Purification of adipoyl-7-amino-3-deacetoxycephalosporanic acid from fermentation broth using stepwise elution with a synergistically adsorbed modulator

Yi Xie[a], Emile Van de Sandt[b], Teun de Weerd[b], N.-H. Linda Wang[a,*]

[a]*School of Chemical Engineering, Purdue University, West Lafayette, IN 47907-1283, USA*
[b]*DSM Anti-Infectives, P.O. Box 1, 2600 MA Delft, The Netherlands*

Abstract

Multicomponent adsorption data of a fermentation broth containing adipoyl-7-amino-3-deacetoxycephalosporanic acid (adipoyl-7-ADCA), a cephalosporin precursor for 7-ADCA, and two key impurities, α-hydroxyadipoyl-7-ADCA and α-aminoadipoyl-7-ADCA were obtained from batch equilibrium and frontal chromatography tests. Amberlite XAD-1600 was chosen as the resin. A rate model was applied to simulate the chromatograms. An alkaline buffer, which by itself has no affinity for the resin, was used as the eluent. The widely used reversed-phase modulator model is inaccurate in explaining the stepwise elution data. A new model, the induced competition model, has been developed to account for apparent retention of the buffer in the presence of adsorbed species. Close agreement between the simulations and the data was achieved with the new model. © 2001 Elsevier Science B.V. All rights reserved.

Keywords: Adsorption isotherms; Adsorption; Mathematical modeling; Induced competition model; Axial dispersion; Mass transfer; Adipoyl-7-amino-3-deacetoxycephalosporanic acid; Cephalosporins; Antibiotics

1. Introduction

Cephalosporins are important antibiotics. Unlike penicillins, cephalosporins are orally absorbable due to their high acid stability and have broad spectra of activity against Gram-positive and Gram-negative bacteria [1,2]. Semi-synthetic cephalosporins are usually obtained by chemical modifications of the side chains at positions 3 and 7 of the nucleus of cephalosporin intermediates. 7-Amino-3-deacetoxycephalosporanic acid (7-ADCA) is one of the important intermediates. For instance, cephalexin can be synthesized from 7-ADCA enzymatically [3,4].

However, the conventional processes for producing 7-ADCA are complex and costly [5]. A simple and cost-effective process has been developed to produce 7-ADCA [5–8]. In this process, a recombinant strain of *Penicillium chrysogenum* has been created to produce adipoyl-7-ADCA (compound A), which is then easily converted to 7-ADCA by removing the adipoyl side chain with a glutaryl acylase. No requirement of organic solvents makes this process environment-friendly [8].

In the fermentation process to produce compound A, two major impurities are formed. As shown in Fig. 1, the two impurities, α-hydroxyadipoyl-7-ADCA (compound B) and α-aminoadipoyl-7-ADCA (compound C), have similar molecular structures to compound A. To obtain pure compound A from the fermentation broth, an efficient purification technique
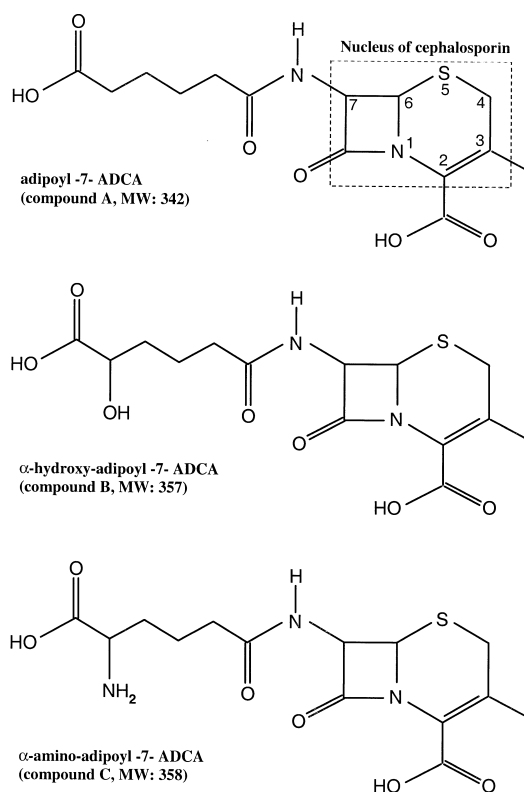
Fig. 1. Molecular structures of adipoyl-7-ADCA (compound A), α-hydroxyadipoyl-7-ADCA (compound B), and α-aminoadipoyl-7-ADCA (compound C). MW = Molecular mass.

is needed. Methods of purification of cephalosporin intermediates have been reviewed by Ghosh et al. [9]. Adsorption chromatography, using reversed-phase materials in particular, has been found to be most successful. In this study, an aromatic polymeric sorbent, Amberlite XAD-1600 (Rohm & Haas), is used to separate compound A from the impurities. Adsorption equilibrium parameters and mass-transfer parameters of these cephalosporin intermediates on Amberlite XAD-1600 have not been available from the literature.

In a multicomponent system, individual adsorbing species interfere with each other in the nonlinear isotherm range. The simplest model to describe the interference behavior is the well-known Langmuir isotherm model [10,11]. The Freundlich–Langmuir isotherm model, a combination of the Freundlich and Langmuir isotherm models often gives a better fit to data [12]. However, the Freundlich–Langmuir iso-

therm model is an empirical model and is not thermodynamically consistent [13]. Both the Langmuir isotherm model and the Freundlich–Langmuir isotherm model are applied to predict the batch equilibrium adsorption data of mixtures of compounds A, B and C on Amberlite XAD-1600.

The dynamic adsorption behavior of the ternary system is studied using packed columns filled with Amberlite XAD-1600. Seven frontal experiments are conducted. A rate model is used to simulate the chromatograms.

An alkaline buffer is used to elute adsorbed solutes. When the buffer is loaded into the column, a pH gradient inside the column forms. By carefully selecting the buffering species, Frey et al. [14], Narahari et al. [15], and Bates and Frey [16] were able to separate and concentrate proteins. In their study, a pH gradient is formed by the buffering species adsorbed on the resin. The buffer used in this study, however, does not adsorb onto the resin. Instead, it interacts with compound A and the impurities and modifies their affinities. The reversed-phase modulator model, which has been extended from linear systems [17,18] to nonlinear systems by Antia and Horváth [19], is applied to simulate the elution histories. However, the simulated elution peaks of compound A are ahead of the experimental peaks and have different shapes.

A new model, the induced competition model, is developed to explain the elution behavior. According to this model, the modulator (the buffer in this study), which by itself has no affinity for the resin, acquires affinity in the presence of certain adsorbed solutes (compounds A, B and C in this study). The modulator then competes with and displaces the adsorbed solutes. Simulation results with this new model closely agree with the experimental data. The chromatography model and model parameters will be used for the design and optimization of continuous processes in a subsequent study.

2. Theory

2.1. Correlation of batch equilibrium data

Equilibrium isotherm adsorption data of mixtures are needed to understand the interference phenomena

in batch and continuous chromatography. In this study, the adsorption data of compounds A, B and C on Amberlite XAD-1600 are obtained from batch equilibrium tests using a filtered fermentation broth, which contains the three cephalosporin intermediates and other unidentified impurities.

Both the Langmuir isotherm model and the Freundlich–Langmuir isotherm model are applied to fit the adsorption data. These two models are as follows.

2.1.1. The Langmuir isotherm model

$$q_i = \frac{a_i C_i}{1 + \sum_{j=1}^{N} b_j C_j}; \quad i = 1, 2, \ldots, N \tag{1}$$

where q_i and C_i are the concentrations of the ith component in the solid phase and in the liquid phase at equilibrium, respectively; a_i and b_i are the Langmuir isotherm parameters; N is the total number of adsorbed species.

2.1.2. The Freundlich–Langmuir isotherm model

$$q_i = \frac{a_{Fi} C_i^{M_{ai}}}{\beta_i + \sum_{j=1}^{N} b_{Fj} C_j^{M_{bj}}}; \quad i = 1, 2, \ldots, N \tag{2}$$

where a_{Fi}, b_{Fi}, M_{ai}, M_{bi} and β_i are the Freundlich–Langmuir isotherm parameters.

The saturation capacity (a_i/b_i) of each component in the Langmuir isotherm model should be the same, in order to be thermodynamically consistent [20]. The Freundlich–Langmuir isotherm model is empirical and usually gives good fitting, but it is not thermodynamically consistent. SAS (Statistical Analysis Software), which has multi-variable nonlinear regression capabilities, is used to estimate isotherm parameters from multicomponent batch equilibrium data.

2.2. Rate model

A rate model is applied to predict the frontal and elution chromatograms of multicomponent mixtures. For the mobile phase, the mass balance is given by:

$$\frac{\partial C_{bi}}{\partial \tau} = \frac{1}{L^{*2} Pe_{bi}} \cdot \frac{\partial^2 C_{bi}}{\partial \xi^2} - \frac{1}{L^*} \cdot \frac{\partial C_{bi}}{\partial \xi} - 3 \Phi_b St(C_{bi} - C_{pi}|_{r^*=1}) \tag{3}$$

with the boundary and initial conditions:

$$\xi = 0, \quad \frac{\partial C_{bi}}{\partial \xi} = L^* Pe_{bi}(C_{bi} - C_{Fi})$$
$$\xi = 1, \quad \frac{\partial C_{bi}}{\partial \xi} = 0 \tag{4}$$
$$\tau = 0, \quad C_{bi} = 0$$

and the dimensionless groups are defined as:

$$\tau = \frac{u_0}{R_p}t, \qquad \xi = \frac{x}{L}, \qquad L^* = \frac{L}{R_p}$$
$$Pe_b = \frac{u_0 R_p}{E_b}, \quad St = \frac{k_f}{u_0}, \quad \Phi_b = \frac{1 - \varepsilon_b}{\varepsilon_b} \tag{5}$$

where subscript i refers to the ith component, C_b is the concentration (g/l) of the mobile phase, t is time (s), x is the distance (cm) in the axial direction of the column, u_0 is the interstitial velocity (cm/min), E_b is the axial dispersion coefficient (cm²/min), k_f is the film mass-transfer coefficient (cm/min), R_p is the particle radius (cm), $C_{p,r^*=1}$ is the concentration (g/l) at the particle surface, C_F is the feed concentration and L is the column length (cm).

For the stationary phase, the mass balance is given by:

$$\frac{\partial C_{pi}}{\partial \tau} + \Phi_p \sum_{j=1}^{N} \frac{\partial q_i}{\partial C_{pj}} \cdot \frac{\partial C_{pj}}{\partial \tau} = \frac{1}{Pe_{pi}} \cdot \frac{\partial}{r^{*2} \partial r^*} \cdot \left(r^{*2} \cdot \frac{\partial C_{pi}}{\partial r^*} \right) \tag{6}$$

with the boundary and initial conditions:

$$r^* = 0, \quad \frac{\partial C_{pi}}{\partial r^*} = 0$$
$$r^* = 1, \quad \frac{\partial C_{pi}}{\partial r^*} = Sh_i(C_{bi} = C_{pi}) \tag{7}$$
$$\tau = 0, \quad C_{pi} = 0$$

and the dimensionless groups are defined as:

$$r^* = \frac{r}{R_p}, \qquad \Phi_p = \frac{1 - \varepsilon_p}{\varepsilon_p}$$

$$\mathrm{Pe}_p = \frac{u_0 R_p}{D_p^{app}}, \quad \mathrm{Sh} = \frac{k_f R_p}{\varepsilon_p D_p^{app}} \qquad (8)$$

where C_p is the pore phase concentration (g/l), q is the solid-phase concentration (g/l solid volume), r is the distance (cm) in the radial direction of particles, and D_p^{app} is the apparent pore (intra-particle) diffusivity, which is a function of the intrinsic pore diffusivity, D_p and surface diffusivity, D_s (cm^2/min). This function is given by [21]:

$$D_p^{app} = D_p + \frac{1 - \varepsilon_p}{\varepsilon_p} \cdot D_s \cdot \frac{\partial q_i}{\partial C_i} \qquad (9)$$

If the particles in the packed bed are non-porous, the mass balance for the stationary phase can be reduced to:

$$3\mathrm{St}(C_{bi} - C_{pi}|_{r^*=1}) = \sum_{j=1}^{N} \frac{\partial q_i}{\partial C_{pj}} \cdot \frac{\partial C_{pj}}{\partial \tau}\bigg|_{r^*=1} \qquad (10)$$

The computation time for the non-porous model is much shorter than that for the porous model, since a large number of equations associated with the particle phase are skipped. The non-porous model, however, is not as accurate as the porous model for nonlinear isotherm systems. The concentration gradients within particles are ignored and flux into the particle is expressed by an overall mass-transfer coefficient and an average concentration difference. This approximation usually underestimates wave sharpness for nonlinear systems [22].

The above governing equations (Eqs. (3)–(10)) only illustrate the mass balance inside the column. In order to account for dispersion in the extra-column dead volume, additional equations are needed. The extra-column dead volume includes the volume of tubing, connections, and pump chambers. Migliorini et al. [23] have investigated the extra-column dispersion effects on simulated moving bed (SMB) performance. The flow in the extra-column dead volume is described with a second order differential equation which is similar to the column model. However, much additional computational effort is needed, particularly when the extra-column dead volume is very small.

In this study, two simple approaches are used to approximate extra-column dispersion without adding second-order differential equations. One is to use the intra-column axial dispersion by lumping the extra-column dead volume into the column. The interstitial velocity and the total resin volume remain the same, but the column length and inter-particle voidage are increased and the inner diameter of the column is decreased:

$$\varepsilon_b' = \frac{\varepsilon_b + \dfrac{DV}{BV}}{1 + \dfrac{DV}{BV}}$$

$$d' = \sqrt{\frac{\varepsilon_b}{\varepsilon_b'}} d \qquad (11)$$

$$L' = \left(1 + \frac{DV}{BV}\right) \cdot \left(\frac{\varepsilon_b'}{\varepsilon_b}\right) L$$

where L', d', and ε_b' are the column length, inner diameter of the column, and the inter-particle voidage, respectively, after the extra-column dead volume is lumped, DV is the extra-column dead volume, and BV is the bed volume.

A second way to consider extra-column dispersion is to add two imaginary continuous stirred tanks (CSTs) to the column [24] (Fig. 2). Each CST has
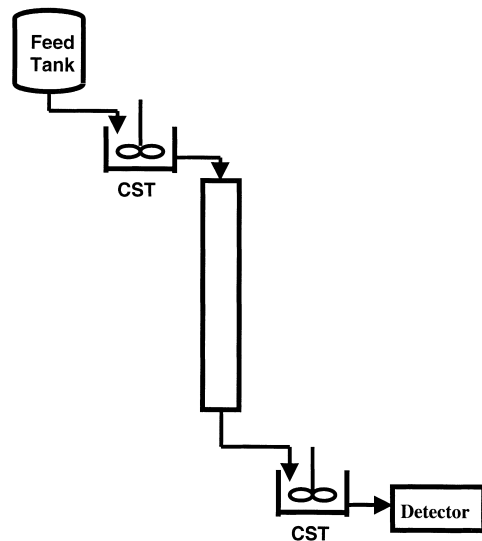

Fig. 2. Diagram of the packed bed with two identical CSTs (one at the inlet, the other at the outlet). The volume of one CST equals one half of total extra-column dead volume.

the volume of half of the total extra-column dead volume. The general CST model is given by:

$$\frac{DV}{2} \cdot \frac{dC_{out}}{dt} = F(C_{out} - C_{in}) \tag{12}$$

where F is the volumetric flow-rate, C_{in} is the concentration at the CST inlet, and C_{out} is the concentration at the CST outlet.

2.3. Models applied in simulations for the elution process

2.3.1. The reversed-phase modulator model

In the elution process, an alkaline buffer (NaHCO$_3$) is used to elute the adsorbed cephalosporin intermediates from the resin. The buffer is considered as an affinity modulator and the reversed-phase modulator model is tried first in simulations to predict the elution curves. The model was given by Antia and Horváth [19] for nonlinear multicomponent systems:

$$q_i = \frac{a_i e^{-S_i C_\phi} C_i}{1 + \sum_{j=1}^{N} b_j e^{-S_j C_\phi} C_j}; \quad i = 1, 2, ..., N \tag{13}$$

where S_i is the modulation parameter for the ith component and C_ϕ is the modulator concentration (g/l). The model parameters, a_i and b_j, are the same as those of the Langmuir isotherm model, which is a special form of Eq. (13) when C_ϕ equals zero.

According to the reversed-phase modulator model, for a given modulator concentration, the extent that compounds lose affinities is determined by the value of the modulation parameter, S_i. Applying the reversed-phase modulator model in simulations for the elution process, one can change the heights and times of the simulated elution peaks of adsorbed compounds by changing the value of S_i. As shown later in the Results and discussion section, it is, however, impossible to use a consistent value of S_i in the simulations to match all experimental data. In most cases, the simulated elution peaks are ahead of the experimental elution peaks. In order to explain the elution behavior of the system in this study, we propose a new model as shown below.

2.3.2. The induced competition model

As shown in Fig. 1, the cephalosporin intermediates have active hydrogens at the end of the adipoyl side chain. The –HCO$_3$ of the buffer (NaHCO$_3$) can react with the active hydrogens of the cephalosporin intermediates. This reaction results in an apparent retention of the buffer in the column and a delay of the elution peak of compound A. The apparent buffer retention can be simulated as if the buffer has certain affinity for the resin in the presence of the other reactants, although the buffer has no affinity for the resin by itself. The apparent affinity of the buffer for the resin depends on the concentrations of other adsorbed species. This behavior can be explained by the following model (see Appendix A for derivation):

$$q_\phi = \frac{\left(\sum_{j=1}^{N} a_{j\phi} C_j\right) C_\phi}{1 + \left(\sum_{j=1}^{N} b_{j\phi} C_j\right) C_\phi + \sum_{j=1}^{N} b_j C_j} \tag{14}$$

$$q_i = \frac{a_i C_i}{1 + \left(\sum_{j=1}^{N} b_{j\phi} C_j\right) C_\phi + \sum_{j=1}^{N} b_j C_j}; \quad i = 1, 2, ... N$$

where $a_{j\phi}$ and $b_{j\phi}$ are model parameters.

According to Eq. (14), the buffer has no affinity in the absence of other compounds ($C_j = 0$), whereas it has apparent affinity in the presence of certain adsorbing compounds. The affinity of the buffer increases as the concentrations of the adsorbing compounds increase, which implies a synergistic adsorption behavior [10]. This synergistic behavior can be shown by the derivatives of q_ϕ with respect to C_i (N is set one for simplicity):

$$\frac{\partial q_\phi}{\partial C_1} = \frac{a_{1\phi} C_\phi}{(1 + b_{1\phi} C_1 C_\phi + b_1 C_1)^2} > 0 \tag{15}$$

On the other hand, the adsorbing compounds lose their affinities after reacting with the buffer and are eluted from the column. The elution can be simulated as if the buffer, which obtains affinity, competes with and displaces the adsorbed compounds. The competitive behavior is shown by:

$$\frac{\partial q_1}{\partial C_\phi} = \frac{-a_1 b_{1\phi} C_1^2}{(1 + b_{1\phi} C_1 C_\phi + b_1 C_1)^2} < 0 \tag{16}$$

Since this model involves an induced adsorption by other compounds and a competition with the adsorbed compounds, it is called the induced competition model.

2.4. Axial dispersion and mass-transfer parameters

To solve the governing equations (Eqs. (3)–(8)), individual mass-transfer parameters (E_b, k_f, D_p^{app}) are needed. These mass-transfer parameters are first estimated from empirical correlations, then modified by comparing the experimental data with the results of model calculations. Dimensionless group analysis will help find the dominant mass-transfer mechanism in this system.

Notice that the aforementioned mass-transfer parameters are related to the Brownian diffusivity (D^{∞}). Therefore, D^{∞} values of compounds A, B and C are first estimated from the Wilke and Chang correlation [25]. The Brownian diffusivity of NaCl is reported by Hritzko et al. [26] using the procedure given by Robinson and Stokes [27]. Then the film mass-transfer coefficient, k_f, is estimated from the Wilson and Geankoplis correlation [28]. The Chung and Wen correlation [29] is used to estimate the axial dispersion coefficient, E_b. The apparent pore diffusivity, D_p^{app}, is estimated from the Mackie and Meares correlation [30] without considering surface diffusion.

2.5. Numerical methods

The numerical solutions of the governing equations and boundary conditions (Eqs. (3)–(8)) have been reported previously [21,31–33]. An orthogonal collocation on finite elements method [34,35] is used to discretize the first and second partial spatial derivatives in both the axial and radial directions. Once the partial differential equations are converted to a system of ordinary differential equations (with respect to time), a time integrator, DASSL [36], is used to integrate in the time domain. To simulate the CSTs, one more equation (Eq. (12)) for each CST is added into the discretized differential equations.

3. Experimental

3.1. Material

The fermentation broth of compound A was obtained from DSM Anti-Infectives (Delft, The Netherlands). Amberlite XAD-1600 was purchased from Rohm & Haas (Spring House, PA, USA). The properties of Amberlite XAD-1600 are listed in Table 1. Pure methanol was purchased from Fisher Scientific (Fairlawn, NJ, USA). Distilled deionized water (DDW) was obtained through a Milli-Q system by Millipore (Bedford, MA, USA). Blue dextran was purchased from Sigma (St. Louis, MO, USA).

3.2. Equipment and analysis

A Pharmacia (Piscataway, NJ, USA) fast protein liquid chromatography (FPLC) system and a small column (12.5×1 cm), which was packed with Amberlite XAD-1600, were used in the experiments to estimate the particle porosity. The FPLC system consists of two pumps (Pharmacia P-500), a liquid chromatography controller (Pharmacia LCC-500), an

Table 1
Properties of Amberlite XAD-1600

Item	Description
Matrix	Macroporous crosslinked polystyrene
Physical form	White beads
Moisture holding capacity	67–75%
Bulk density	608–672 g/l
Fines content	<200 μm: 1% max
Harmonic mean size	400±50 μm
Uniformity coefficient	≤1.25
Surface area	≥800 m^2/g
Porosity	>0.5 ml/ml

injection valve (Pharmacia MV-7), and a fraction collector (Pharmacia Frac-100). Data monitoring and collection were handled by a photodiode array detector (Waters 990) with data collection software.

Samples of the cephalosporin intermediates were analyzed by high-performance liquid chromatography (HPLC). This HPLC system consists of one pump (Waters 510), a tunable single-wavelength detector (Waters 486), and a YMC pack ODS AQ column (150×4.6 mm). The mobile phase consisted of 84% phosphate buffer (pH 6.0) and 16% acetonitrile [6]. The flow-rate of the mobile phase was 1.0 ml/min and the sample injection volume was 3–5 µl. The chromatograms were examined at the wavelength of 260 nm.

A Radiometer CDM80 conductivity detector was used to measure NaCl concentration.

3.3. Procedure

3.3.1. Batch equilibrium tests

A series of solutions was made by diluting the filtered fermentation broth, which contained compounds A, B C and other unidentified impurities. Every 50 ml solution was mixed with 5 g Amberlite XAD-1600 at room temperature (298 K). The solutions and the resins were continuously stirred for 16 h.

3.3.2. Estimation of particle porosity

The small column was pre-equilibrated with pure methanol before a blue dextran pulse was injected. The flow-rate of the mobile phase was 1 ml/min and the pulse size was 200 µl. After elution of the blue dextran pulse, DDW was used to remove methanol from the column. The inter-particle voidage, ε_b, was estimated from the retention time of the blue dextran pulse and the total bed voidage, ε_t, was obtained from the mass center of the DDW breakthrough curve. Then the particle porosity, ε_p, was calculated by:

$$\varepsilon_p = \frac{\varepsilon_t - \varepsilon_b}{1 - \varepsilon_b} \tag{17}$$

3.3.3. Estimation of extra-column dead volume

The extra-column dead volume was estimated from NaCl frontal tests. The column was taken off-line, so that only connecting tubings between the feed tank and the detector were present. The flow-rate was 40 ml/min. The mass center of the breakthrough curve of NaCl provided the retention time of NaCl in the tubings, connections and pump chambers. Then the extra-column dead volume was obtained by multiplying the retention time by the flow-rate. The dead volume was also confirmed by the mass center of the washing curve of NaCl.

3.3.4. Estimation of inter-particle voidage for the preparative column

The preparative column used to study the dynamic adsorption processes of the fermentation broth was packed with Amberlite XAD-1600. The column volume and resin particle size are listed in Table 2. The resin packed in the preparative column was from the same lot as in the small column. Therefore, the particle porosity estimated from the small column can be used in the preparative column. Frontal tests of NaCl, which does not adsorb onto the resin, were conducted. The flow-rate was 40 ml/min. The total bed voidage was obtained from the mass center of the breakthrough curve of NaCl (the extra-column dead volume was subtracted). Then the inter-particle voidage of the preparative column was calculated from Eq. (17).

3.3.5. Chromatography tests with the fermentation broth

Seven chromatography tests with the filtered fermentation broth were performed. Each test included three steps: loading, washing, and elution. Deionized water was used to wash the column after loading. Hydrogencarbonate buffer (NaHCO$_3$) was chosen as the eluent. The flow-rate, loading time, washing time, and eluent concentration for each experiment are listed in Table 3.

Table 2
Preparative column properties

	Bed volume (ml)	Dead volume (ml)	ε_b	ε_p	R_p (µm)
Column 1	940	86.0	0.457	0.55	198
Column 2	1650	86.0	0.457	0.55	198

Table 3
Operating parameters of frontal experiments

	Flow-rate (ml/min)	Loading time (min)	Washing time (min)	Concentration of buffer (M)
Run 1	23	342	120	0.2
Run 2	63	126	43	0.2
Run 3	110	74	24	0.2
Run 4	156	53	16	0.2
Run 5	50	100	96	0.1
Run 6	50	88	96	0.2
Run 7	50	100	95	0.3

4. Results and discussion

4.1. Batch equilibrium tests

The data of batch equilibrium tests are plotted in

Compound A ○○○ Compound B ✳✳✳ Compound C +++
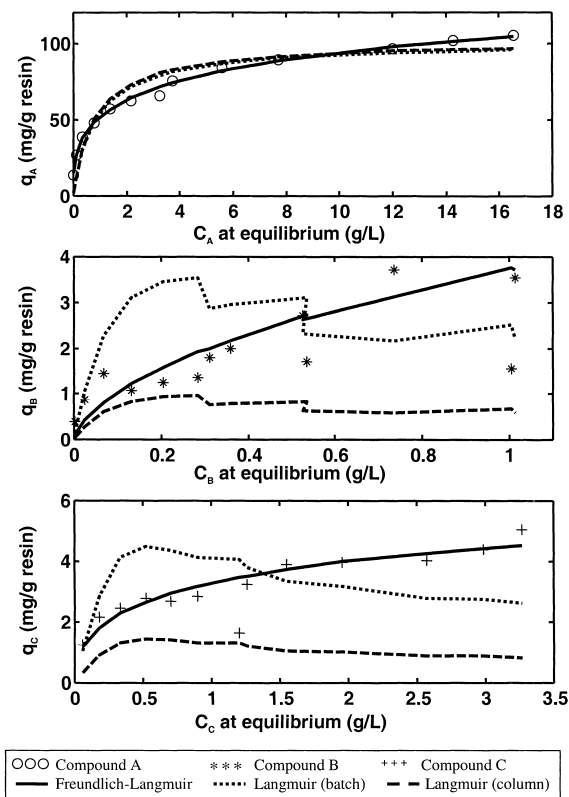Freundlich-Langmuir —— Langmuir (batch) ····· Langmuir (column) – –

Fig. 3. Isothermal adsorption data of batch equilibrium tests with model predictions. Symbols are experimental data and lines are model predictions.

Fig. 3. The abscissa of Fig. 3 is the concentration of each species at equilibrium and the coordinate is the amount of adsorbed species accordingly. Note that each data point indicates the liquid phase concentrations of all three species at equilibrium. For example, each point in the compound A adsorption curve represents not only the concentration of compound A at equilibrium, which is shown in the abscissa, but also the concentrations of the associated compounds B and C at equilibrium.

The data of the batch equilibrium tests were fit with the Langmuir (Eq. (1)) and the Freundlich–Langmuir (Eq. (2)) isotherm models. The estimated isotherm parameters are listed in Table 4. Since only the discrete equilibrium concentrations of the experiments are used in the calculation, the model predicted curves are discontinuous (Fig. 3). The entire continuous model predicted curves lie in a four-dimensional space, which cannot be plotted. As

Table 4
Isotherm parameters of compounds A, B and C

		A	B	C
Freundlich–Langmuir	a_{Fi} [a]	241	21.3	16.1
	b_{Fi}	0.164	0.580	0.0689
	M_{ai}	0.327	0.655	0.411
	M_{bi}	0.327	0.00222	0.982
	β_i	1.00	1.00	1.00
Langmuir				
From batch	a_i [a]	356	134	49.6
	b_i	1.30	0.491	0.181
From column	a_i [a]	356	36	16
	b_i	1.30	0.50	0.10

[a] Isotherm parameters, a_i and a_{Fi}, are based on solid volume of particles.

shown in Fig. 3, the Freundlich–Langmuir isotherm model predicts the batch equilibrium data much better than the Langmuir isotherm model.

Note that the fermentation broth used in the batch equilibrium tests contains not only the three major compounds, A, B and C, but also some other unidentified compounds of which concentrations are unknown. However, only compounds A, B and C are considered in both the Langmuir and the Freundlich–Langmuir isotherm models. For this reason, the estimated isotherm parameters by fitting the batch equilibrium tests data are not the intrinsic parameters but the effective parameters. If these effective parameters are applied in the simulations of chromatography tests, the simulated chromatograms deviate from the experimental data significantly as shown below.

The adsorption mechanism of compounds A, B and C on Amberlite XAD-1600 has not been available from the literature. The equilibrium data of cephalosporin C on Amberlite XAD-16, which has the same internal structure as Amberlite XAD-1600 according to the product data sheet from Rohm & Haas, however, has been reported by Chaubal et al. [37]. According to their study, the hydrophobic interactions between the planar region of cephalosporin C and the phenyl groups of Amberlite XAD-16 are the major driving forces for adsorption. Since compounds A, B and C have similar molecular structures as cephalosporin C, their adsorption on Amberlite XAD-1600 could also be due to hydrophobic interactions. Therefore, the adsorption parameters reported in Table 4 show a strong correlation between solute affinity and hydrophobicity. Molecular structures indicate that compound A is more hydrophobic than the other two impurities (Fig. 1), hence it has the highest affinity among the three cephalosporin intermediates (Table 4).

4.2. Column characterization

Before the chromatography tests with the cephalosporin intermediates, characterization of the resin and the column were conducted. The particle porosity, ε_p, the inter-particle voidage, ε_b, and the extra-column dead volume were estimated. The effects of extra-column dispersion were studied.

The particle porosity was estimated from the aforementioned small column. The value of ε_p is listed in Table 2. This value is consistent with that provided by Rohm & Haas (Table 1). The values of the extra-column dead volume and the inter-particle voidage estimated from NaCl frontal tests are listed in Table 2.

The extra-column dispersion effects were studied by lumping the extra-column dead volume into the column and by treating the extra-column dead volume as CST, respectively. The simulation results based on the two methods are plotted with the experimental data in Fig. 4. In the simulations, the mass-transfer parameters are calculated from the correlations and listed in Table 6.

As shown in Fig. 4, the mass center times of NaCl breakthrough and washing curves can be predicted by either lumping the extra-column dead volume into the column or using CSTs. However, the experimental data show more spreading than the simulated curves with the lumped extra-column dead volume (dashed lines). This indicates that the extra-column dispersion is significant in this system. If the CST approach is applied, the simulation results (solid lines) are in close agreement with the experimental data. Therefore, the CST approach is adopted and used in later simulations for the frontal tests with the filtered fermentation broth.
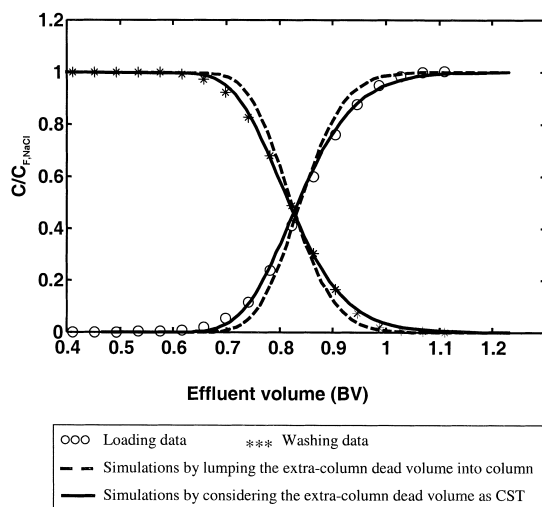

Fig. 4. NaCl frontal and washing tests. Symbols are experimental data and lines are simulation results.

4.3. Chromatography tests with the fermentation broth

4.3.1. Loading and washing processes (frontal tests)

4.3.1.1. Isotherm parameters

The three-component Freundlich–Langmuir isotherm model with model parameters obtained from the batch equilibrium tests was applied to simulations for frontal tests first, since this model closely predicts the batch adsorption data. However, the numerical solution is hard to converge. This can be explained by the Jacobian matrix of the Freundlich–Langmuir isotherm model and the mass balance equation (Eq. (6)). The Jacobian matrix of the Freundlich–Langmuir isotherm model can be derived from Eq. (2):

$$\frac{\partial q_i}{\partial C_i} = \frac{a_i \cdot \left[M_{ai} \cdot \left(\beta_i + \sum_{j=1}^{N} b_j C_j^{M_{bj}} \right) - M_{bi} b_i C_i^{M_{bi}} \right]}{\left(\beta_i + \sum_{j=1}^{N} b_j C_j^{M_{bj}} \right)^2} \cdot C_i^{M_{ai}-1}$$

$$\frac{\partial q_i}{\partial C_j} = \frac{-a_i b_j M_{bj} C_i^{M_{ai}}}{\left(\beta_i + \sum_{j=1}^{N} b_j C_j^{M_{bj}} \right)^2} \cdot C_j^{M_{bj}-1}$$

(18)

According to Eq. (18), if the concentration is close to zero and M_a or M_b is greater than zero and much less than unity, then $\partial q/\partial C$ approaches infinity. Moreover, as $\partial q/\partial C$ approaches infinity, Eq. (6) indicates that the concentration gradient inside the particle approaches infinity as well. Consequently, the numerical solution is difficult to converge. In the frontal tests, the column was clean (concentration equals zero) before loading. In addition, values of M_a and M_b of all three species are less than one. In particular, M_b of compound B is much less than one (Table 4). Therefore, no converged solution with these parameters using the porous model was obtained.

Since the solution with the Freundlich–Langmuir isotherm model is difficult to converge, the Langmuir isotherm model was then tried. When the Langmuir isotherm parameters obtained from the batch equilibrium tests (defined as batch isotherms) are applied, the simulated chromatograms of the major component, compound A, are in reasonable agreement with the experimental data (Fig. 5a). The simulated chromatograms of the two key impurities, however, are substantially different from the experimental data (Fig. 5a). The Langmuir isotherms of the impurities were modified such that the simulated frontal curves closely agree with the data (Fig. 5b). The modified isotherms are listed in Table 4. Note that the axial dispersion and mass-transfer parameters were adjusted simultaneously. The detailed procedure to adjust the axial dispersion and mass-transfer parameters is explained below.

The effective Langmuir isotherm parameters obtained by fitting the frontal chromatograms (defined as column isotherms) were used to calculate the amount of adsorbed species of the batch equilibrium tests. The results of the Langmuir isotherm model prediction with the column isotherms are shown in Fig. 3 (dashed lines). For the major component, compound A, there is little difference between the model predictions with the batch isotherms and with the column isotherms. For the two impurities, compounds B and C, the effective capacities determined from the frontal tests are substantially lower than those determined from the batch equilibrium tests.

Note that the frontal tests were carried out with the feed at high concentrations, which were close to the upper limit of the equilibrium concentration range of the batch equilibrium tests. Recall that the fermentation broth contains other unidentified compounds and the solutions used in the batch equilibrium tests were diluted. The competition for adsorption sites from the unidentified compounds is less significant in the batch equilibrium tests than in the frontal tests. In addition, the Langmuir isotherm model is not accurate for the batch equilibrium data and underestimates the data at high equilibrium concentrations (dotted lines in Fig. 3). For these reasons, the estimated amount of the adsorbed impurities based on the column isotherms at one feed concentration is lower than the batch equilibrium data over the entire range of equilibrium concentrations.

Once the Langmuir isotherm parameters are obtained, one can repeat the simulations with the Freundlich–Langmuir isotherm model to check the argument about the aforementioned numerical convergence issue. First, the numerical solution converges if the non-porous model is applied with the
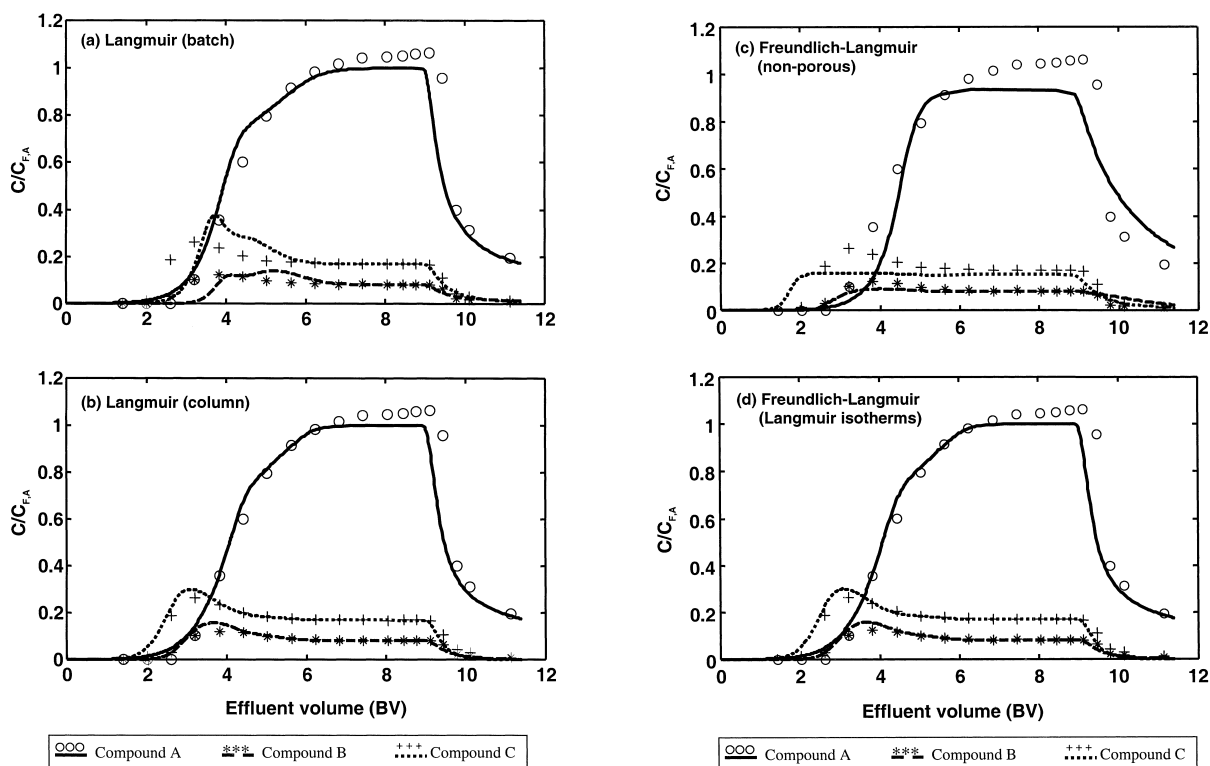
Fig. 5. Experimental data and simulations of loading and washing processes of run 2 with different isotherms. $C_{F,A}$ stands for the feed concentration of compound A and BV stands for bed volume. Symbols are experimental data and lines are simulation results. (a) Simulations with the Langmuir isotherm parameters estimated from the batch equilibrium tests. (b) Simulations with the Langmuir isotherm parameters estimated by fitting the experimental data of fixed bed. (c) Simulations with the Freundlich–Langmuir isotherm model using the non-porous model. (d) Simulations with the Freundlich–Langmuir isotherm model using the porous model, in which the Langmuir isotherm parameters same as those in (b) are used.

Freundlich–Langmuir isotherm model. The simulation results are shown in Fig. 5c. In this simulation, the isotherm parameters of the Freundlich–Langmuir model are from the batch equilibrium tests and the axial dispersion coefficients are the same as those in the simulations from which Fig. 5a and b were generated. The pore diffusivities are lumped into the film mass-transfer coefficients. However, the simulated chromatograms do not agree with the data; particularly, no roll-up of the concentrations of compounds B and C is shown by the simulations.

Second, if the Freundlich–Langmuir isotherm model with the Langmuir column isotherms is applied (i.e., $a_{Fi}=a_i$, $b_{Fi}=b_i$, and β_i, M_{ai}, and M_{bi} are set to one), the numerical solution with porous model converges, since the values of M_{ai} and M_{bi} equal one. As expected, the simulated chromato-

grams (with the Freundlich–Langmuir model) in Fig. 5d are identical to those (with the Langmuir model) in Fig. 5b. These two simulation tests verify the previous explanation of why the solution with the porous model is difficult to converge if the Freundlich–Langmuir model with the isotherm parameters estimated from the batch equilibrium tests is used.

4.3.1.2. Axial dispersion and mass-transfer parameters

The aforementioned correlations in the Theory section provide rough estimations of axial dispersion and mass-transfer parameters. Based on these estimated parameters, one can calculate the dimensionless numbers in Eqs. (3) and (6) and analyze the contributions of different mass-transfer mechanisms.

The dimensionless groups, Pe_b, St, and $1/Pe_p$,

Table 5
Values of dimensionless groups for compound A

	Run 1	Run 2	Run 3	Run 4	Runs 5–7
Re	0.182	0.498	0.870	1.23	0.188
Pe_b	0.224	0.227	0.228	0.232	0.224
St	0.0226	0.0115	0.00794	0.00629	0.0220
$1/Pe_p$	0.000711	0.000260	0.000149	0.000105	0.000687

indicate, respectively the importance of axial dispersion, film mass-transfer, and apparent pore diffusion on wave spreading. The values of these dimensionless groups are listed in Table 5. Apparent pore diffusion is found to be the dominant mass-transfer mechanism, since the values of $1/Pe_p$ are much smaller than those of Pe_b and St (Table 5). As the Reynolds number increases, the contributions of apparent pore diffusion and film mass-transfer to the overall mass-transfer mechanism increase, whereas those of axial dispersion decrease (Table 5). Therefore, the frontal chromatograms at high flow-rates should be used for D_p^{app} estimation and the frontal

chromatograms at low flow-rates should be used for E_b estimation.

The pore diffusivities obtained from fitting the data of the frontal tests are smaller than those estimated from the Mackie and Meares correlation (Table 6). The Mackie and Meares correlation has been used to estimate pore diffusivities for dilute solutions [30]. However, in the frontal tests, the feed concentrations are quite high. Furthermore, the pore diffusivities obtained from fitting the data of the frontal tests are apparent pore diffusivities, which may include both pore diffusivities and surface diffusivities as shown in Eq. (9). Therefore, it is

Table 6
Axial dispersion and mass-transfer parameters and numerical parameters used in simulations

	Axial dispersion and film mass-transfer coefficients					
	Run 1	Run 2	Run 3	Run 4	Runs 5–7	NaCl frontal
E_b (cm^2/min)	23.8	64.2	111	156	0.492	0.809
k_f (cm/min)						
A	0.121	0.170	0.204	0.230	0.123	–
B	0.120	0.168	0.202	0.227	0.121	–
C	0.120	0.167	0.202	0.226	0.121	–
Buffer	0.200	0.280	0.338	0.379	0.203	–
NaCl	–	–	–	–	–	0.314

	Brownian diffusivities and apparent pore diffusivities				
	A	B	C	Buffer	NaCl
$D^\infty \cdot 10^4$ (cm^2/min)	2.90	2.84	2.84	6.15	9.20
$D_p^{app} \cdot 10^4$ (cm^2/min)					
From correlation	0.758	0.742	0.744	1.61	2.41
From fitting	0.24	0.70	0.50	0.51	–

	Numerical parameters				
	Axial element number	Collocation points	Particle points	Δt, max	Absolute tolerance	Relative tolerance
	200	4	3	0.1	$5 \cdot 10^{-4}$	$1 \cdot 10^{-4}$

expected that the pore diffusivities deviate from the prediction of the Mackie and Meares correlation.

As shown in Table 6, the values of D_p^{app} of the three species are different ($D_{p,A}^{app} < D_{p,C}^{app} < D_{p,B}^{app}$), although these three species have similar molecular structures. The parallel diffusion model (Eq. (9)), which includes both pore diffusion and surface diffusion, can explain this phenomenon. In the frontal chromatograms, the species with the lowest affinity, compound C, only "sees" compound C; compound B "sees" compounds B and C; and compound A "sees" all three of them. Therefore, the partial derivatives of q_i over C_i in Eq. (9) for the three components can be written as:

$$\frac{\partial q_A}{\partial C_A} = \frac{a_A(1 + b_B C_B + b_C C_C)}{(1 + b_A C_A + b_B C_B + b_C C_C)^2}$$

$$\frac{\partial q_B}{\partial C_B} = \frac{a_B(1 + b_C C_C)}{(1 + b_B C_B + b_C C_C)^2} \qquad (19)$$

$$\frac{\partial q_C}{\partial C_C} = \frac{a_C}{(1 + b_C C_C)^2}$$

The values of calculated $\partial q_i / \partial C_i$ are in the sequence of $\partial q_B / \partial C_B > \partial q_C / \partial C_C > \partial q_A / \partial C_A$. This sequence is consistent with that of the values of the apparent pore diffusivities (Table 6). Notice that the intrinsic D_p and D_s values of the three species are assumed to be the same, since the three species have similar molecular structures.

The axial dispersion and mass-transfer parameters and numerical parameters used in simulations are listed in Table 6. With these parameters and the isotherm parameters estimated from the frontal test of run 2, simulated chromatograms of the loading and washing processes are in close agreement with the data of experiments at different flow-rates (Fig. 6).

4.3.2. Elution process

As pointed out by Snyder et al. [18], the steeper the eluent gradient, the more the eluted bands are compressed. This indicates that a stepwise elution, which has the steepest gradient, would result in the highest eluate concentration [38]. Highly concentrated compound A is needed for further chemical conversion; therefore, a stepwise elution procedure is applied. The eluted curves were simulated with two
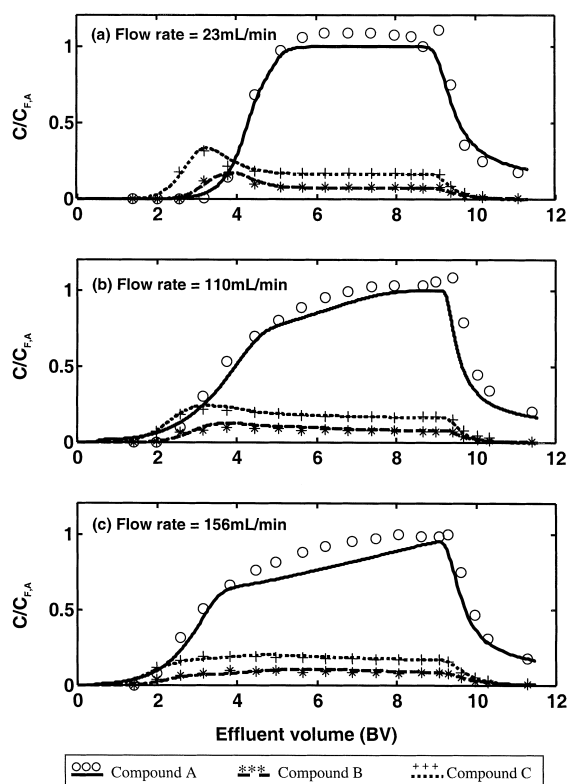

Fig. 6. Simulations and experimental data of loading and washing processes of runs 1, 3 and 4. Symbols are experimental data and lines are simulation results.

models: the reversed-phase modulator model (Eq. (13)) and the induced competition model (Eq. (14)).

4.3.2.1. Reversed-phase modulator model

In order to obtain the modulation parameter in Eq. (13), S_i, a series of simulations with different values of S_i were carried out for the elution process of experiment run 2. The choice of run 2 is arbitrary. As shown in Fig. 7, the simulated elution peaks of compound A are always ahead of the experimental peak in a wide range of S_i. Since it is impossible to fit the exit time of the elution fronts of compound A, the best-fitted modulation parameter, S_i, was estimated by comparing the height of the simulated elution peak of compound A with the experimental data. Note that the modulation parameter, S_i, is assumed to be the same for compounds A, B and C, since they have similar molecular structures. In addition, a very small amount of compounds B and
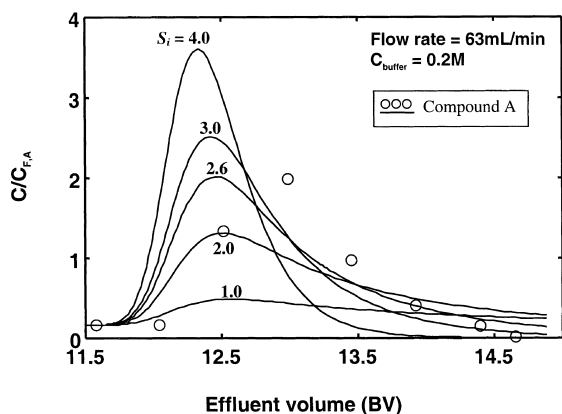
Fig. 7. Simulations with the reversed-phase modulator model and experimental data of the elution process of run 2. Symbols are experimental data and lines are simulation results. The number associated with each curve is the value of S_i used in each simulation.

C remains in the column after the washing process; thus the values of S_i for compounds B and C have little effect on the simulations.

According to the reversed-phase modulator model, the value of S_i should be independent of flow-rate and modulator concentration. For further comparison, the estimated S_i from run 2 was applied in simulations for other runs 1, 3, and 4, in which the buffer concentrations are the same as in run 2 but the flow-rates are different. As shown in Fig. 8, the simulated elution peaks exit the column earlier than the experimental elution peaks, although the heights of the simulated elution peaks agree with the experimental data. Furthermore, in order to match the elution peak heights of the experiments at different buffer concentrations (runs 5–7), the values of the best-fitted S_i values are different. (Fig. 9 and Table 7).
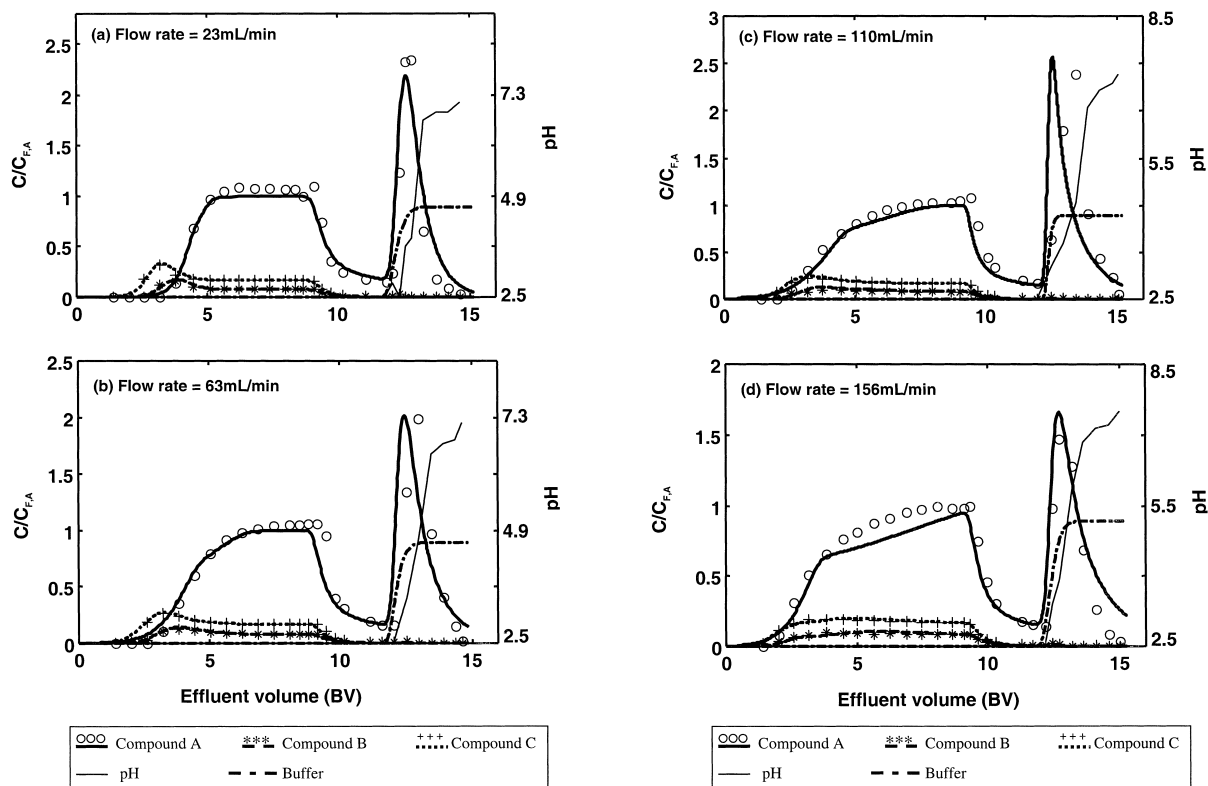

Fig. 8. Simulations with the reversed-phase modulator model and experimental data of runs 1–4. Symbols are experimental data and lines are simulation results. The buffer concentration is 0.2 M for each of the four runs.
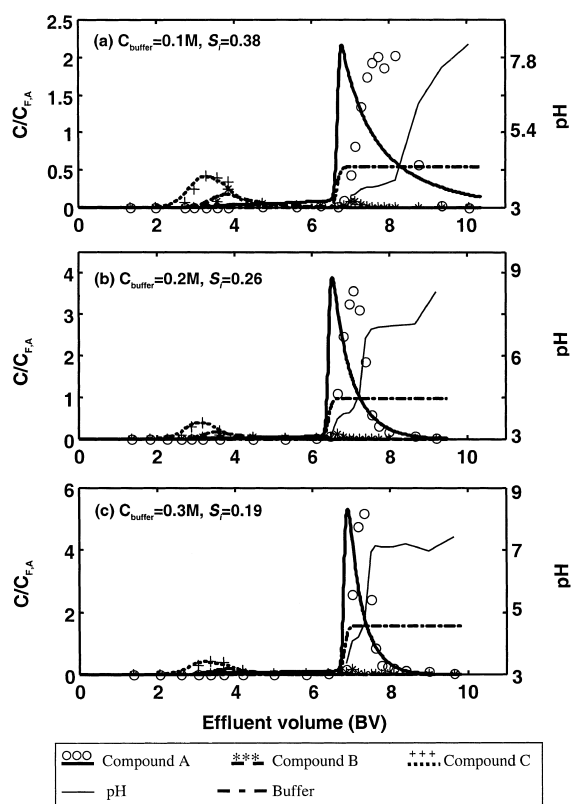
Fig. 9. Simulations with the reversed-phase modulator model and experimental data of runs 5–7. Symbols are experimental data and lines are simulation results.

Besides the elution peaks of compound A, the simulations also provide the buffer breakthrough curves. Since no experimental data of the buffer concentration in the effluent is available, pH would be a good indicator for the buffer breakthrough. Figs. 8 and 9 show that the breakthrough curves of pH

Table 7
Reversed-phase modulator and induced competition model parameters

		Concentration of buffer (M)		
		0.1	0.2	0.3
Reversed-phase modulator model	S_i	0.38	0.26	0.19
Induced competition model	$a_{i\phi}$ [a]	80	80	80
	$b_{i\phi}$	1.0	1.0	1.0

[a] Values are based on solid volume of particles.

(experimental data) lag behind the simulated buffer breakthrough curves, which implies that the buffer behaves like a solute with a nonzero affinity. However, in the absence of other compounds, the buffer has no affinity. In order to describe these phenomena, a new model was developed in the Theory section. The comparison of the simulations with the new model and the experimental data is shown as below.

4.3.2.2. Induced competition model

Following the same procedure as applied to compare the simulations using the reversed-phase modulator model, we estimated the model parameters of the induced competition model (Eq. (14)) by fitting the data of one experiment (run 2) and applied the same model parameters in the simulations for the other experiments. The extent of interactions between the buffer and other compounds is indicated by the model parameters. The model parameters for each component are assumed to be the same for the same reasons mentioned above.

The simulation results with the induced competition model are shown in Figs. 10 and 11. Compared with Figs. 8 and 9, the simulated elution curves of compound A in Figs. 10 and 11 show better agreement with the experimental data. The same model parameters can be applied to all seven experiments (of different buffer concentrations and flow-rates). The spreading of the fronts and sharpness of the tails of the elution curves can be well predicted by the model. According to the induced competition model, the buffer is retained in the column in the presence of compound A. Therefore, the buffer fronts are delayed and spread (comparing Fig. 8 with Fig. 10 and Fig. 9 with Fig. 11). This also results in the spreading of the fronts of compound A elution peaks. On the other hand, as compound A is displaced, the concentration of the adsorbed compound A decreases. The affinity of the buffer is reduced according to Eq. (15). Moreover, the buffer, which comes into the column later, does not "see" compound A. Thus the buffer behind the compound A peaks displaces the buffer in front of the compound A peaks resulting in roll-up of the buffer concentration and the sharp tails of the compound A peaks (Figs. 10 and 11).

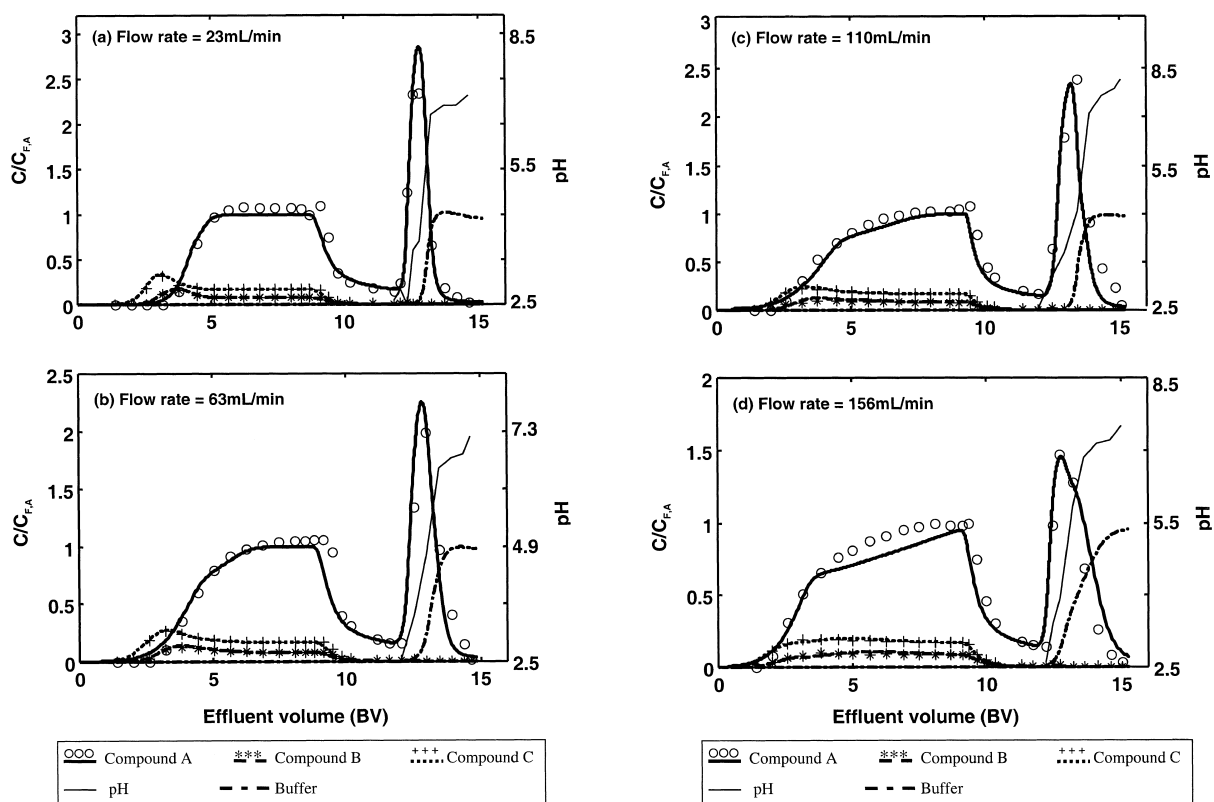As shown previously in Figs. 8 and 9, if the

Fig. 10. Simulations with the induced competition model and experimental data of runs 1–4. Symbols are experimental data and lines are simulation results.

reversed-phase modulator model is applied, the simulated buffer breakthrough curves are ahead of the pH breakthrough curves. When the induced competition model is applied, the mass centers of the simulated buffer fronts are consistent with the pH breakthrough curves (Figs. 10 and 11). This indicates the induced competition model can well predict the apparent retention of the buffer.

5. Conclusions

Multicomponent adsorption data of a fermentation broth, which contains the target product, adipoyl-7-ADCA (compound A), two key impurities, α-hydroxyadipoyl-7-ADCA (compound B) and α-amino-adipoyl-7-ADCA (compound C), and other uniden-

tified impurities on Amberlite XAD-1600 were obtained from batch equilibrium and frontal tests.

The Langmuir isotherm model and the Freundlich–Langmuir isotherm model were used to fit the batch equilibrium experimental data. The Freundlich–Langmuir isotherm model can predict the data closely whereas the prediction of the Langmuir isotherm model deviates from the data substantially.

A rate model was used to simulate chromatograms of frontal tests with the fermentation broth. If the porous rate model is applied with the Freundlich–Langmuir isotherm model, the numerical solution is difficult to converge. This is due to the small values of M_a and M_b (much less than one but greater than zero) for this system.

The Langmuir isotherms estimated from the batch equilibrium tests were modified after comparing the simulated chromatograms with the experimental
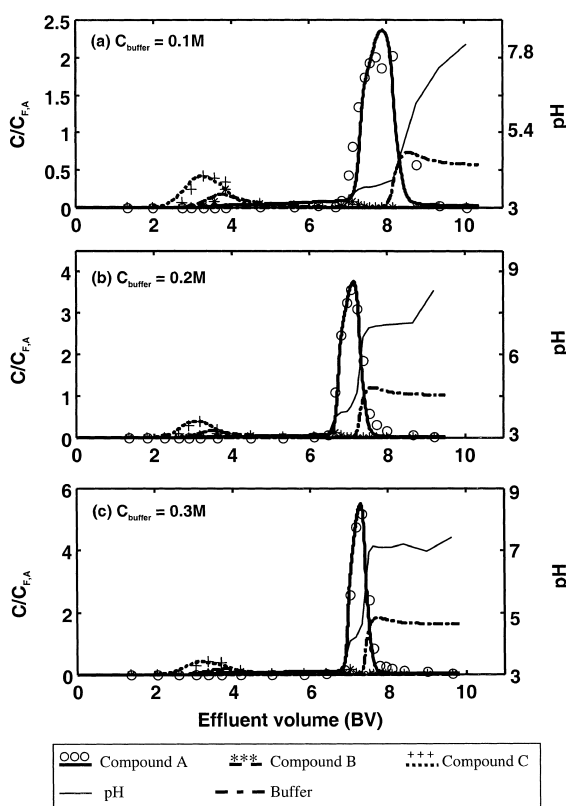
Fig. 11. Simulations with the induced competition model and experimental data of runs 5–7. Symbols are experimental data and lines are simulation results.

data. The simulated chromatograms with the modified isotherms are in close agreement with the data of all seven frontal experiments.

The extra-column dispersion was simulated by lumping the extra-column dead volume into the column and using two imaginary CSTs, whose volume is half of the extra-column dead volume. The CST approach was found to be better for simulating the extra-column dispersion.

Axial dispersion and mass-transfer parameters were first estimated from correlations and then modified by comparing the simulated chromatograms with the experimental data. Intra-particle diffusion is the dominant mass-transfer mechanism in the system of this study according to the dimensionless group analysis, which also indicates that the chromatograms at low flow-rate are better suited for estima-

tion of the axial coefficients whereas the chromatograms at high flow-rate for estimation of the pore diffusivities. The parallel pore and surface diffusion model can explain why the values of the apparent pore diffusivities are in the order of $D_{p,A}^{app} < D_{p,C}^{app} < D_{p,B}^{app}$.

The reversed-phase modulator model is inaccurate in explaining the experimental data of the stepwise elution processes. The best-fitted parameter of this model changes with the modulator (buffer) concentration.

A new model, the induced competition model, has been developed. According to this model, the modulator gains affinity in the presence of other compounds (synergistic behavior) and competes with the adsorbed solutes. Simulated elution curves of the target product, compound A, closely agree with the data of experiments at five different flow-rates (23–156 ml/min) and three different buffer concentrations (0.1–0.3 *M*). The induced competition model and the rate model will be applied to design, scale up, and optimize continuous separation processes for production in the future study.

6. Nomenclature

a	Langmuir isotherm parameter (based on solid volume of particles)
a_F	Freundlich–Langmuir isotherm parameter (based on solid volume of particles)
$a_{i\phi}$	Induced competition parameter (1/g, based on solid volume of particles)
b	Langmuir isotherm parameter (1/g)
b_F	Freundlich–Langmuir isotherm parameter (1/g)
$b_{i\phi}$	Induced competition parameter (l^2/g^2)
BV	Bed volume
C	Liquid phase concentration (g/l)
CST	Continuous stirred tank
D_p^{app}	Apparent pore diffusivity (cm^2/min)
D_p	Intrinsic pore diffusivity (cm^2/min)
D_s	Intrinsic surface diffusivity (cm^2/min)
DV	Dead volume
D^∞	Brownian diffusivity (cm^2/min)
E_b	Axial dispersion coefficient (cm^2/min)
k_f	Film mass transfer coefficient (cm/min)
L	Column length (cm)

L^*	Dimensionless column length (L/R_p)
M_a	Freundlich–Langmuir isotherm parameter
M_b	Freundlich–Langmuir isotherm parameter
Pe_b	Peclet number for mobile phase ($u_0 R_p / E_b$)
Pe_p	Peclet number for pore phase ($u_0 R_p / D_p^{app}$)
q	Solid-phase concentration (g/l solid volume of particles)
r	Distance in the radial direction of particle (cm)
r^*	Dimensionless distance in the radial direction of particle (r/R_p)
Re	Reynolds number ($2R_p u_0 \rho / \mu$)
R_p	Radius of particles (cm)
S	Reversed-phase modulation parameter
Sh	Sherwood number ($k_f R_p / \varepsilon_p D_p^{app}$)
St	Stanton number (k_f / u_0)
x	Distance in the axial direction of column (cm)
u_0	Interstitial velocity (cm/min)

Greek letters

β	Freundlich–Langmuir isotherm parameter
ε_b	Inter-particle voidage
ε_p	Particle porosity
ε_t	Total bed voidage
Φ	Phase ratio (defined in Eqs. (5) and (8))
μ	Mobile phase viscosity (cP)
ρ	mobile phase density (g/ml)
τ	Dimensionless time [$(u_0/R_p)t$]
ξ	Dimensionless distance in the axial direction of column (x/L)

Subscripts

A	Adipoyl-7-ADCA (compound A)
B	α-Hydroxyadipoyl-7-ADCA (compound B)
C	α-Aminoadipoyl-7-ADCA (compound C)
b	Mobile phase
F	Feed
p	Pore phase
i	The ith component
φ	Modulator (buffer)

Appendix A. Derivation of the induced competition model

A kinetic derivation which is similar to that for the Langmuir isotherm model is performed. In order to simplify the procedure, only the modulator (1) and one other component (2) are considered. The kinetic sorption equations of the two species are as follows:

$$\frac{\partial q_1}{\partial t} = (k_{a1} C_2) \cdot \left(1 - \frac{q_1}{q_m} - \frac{q_2}{q_m}\right) \cdot C_1 - k_{d1} q_1$$
$$\frac{\partial q_2}{\partial t} = k_{a2} \cdot \left(1 - \frac{q_1}{q_m} - \frac{q_2}{q_m}\right) \cdot C_2 - k_{d2} q_2 \quad \text{(A.1)}$$

where k_a and k_d are adsorption and desorption rate constants, respectively and q_m is the maximum resin capacity. Notice that the adsorption rate constant for the modulator, k_1, has significance only when C_2 is present. As adsorption and desorption reach equilibrium, Eq. (A.1) becomes:

$$(k_{a1} C_2) \cdot \left(1 - \frac{q_1}{q_m} - \frac{q_2}{q_m}\right) \cdot C_1 - k_{d1} q_1 = 0$$
$$k_{a2} \cdot \left(1 - \frac{q_1}{q_m} - \frac{q_2}{q_m}\right) \cdot C_2 - k_{d2} q_2 = 0 \quad \text{(A.2)}$$

Eq. A.2 is solved and q_1 and q_2 are given by:

$$q_1 = \frac{a_{21} C_2 C_1}{1 + b_{21} C_2 C_1 + b_2 C_2}$$
$$q_2 = \frac{a_2 C_2}{1 + b_{21} C_2 C_1 + b_2 C_2} \quad \text{(A.3)}$$

where:

$$a_{21} = q_m b_{21} \quad b_{21} = \frac{k_{a1}}{k_{d1}} \cdot \frac{1}{q_m}$$
$$a_2 = q_m b_2 \quad b_2 = \frac{k_{a2}}{k_{d2}} \cdot \frac{1}{q_m} \quad \text{(A.4)}$$

Eq. (A.3) can be easily expanded to the form of Eq. (14) for N components and one modulator.

References

[1] A. Smith, in: M.M. Young (Ed.), Comprehensive Biotechnology – The Principles, Applications and Regulations of Biotechnology, Pergamon Press, New York, 1985.

[2] R.C. Moellering Jr., Oral Cephalosporins, Karger, Basel, 1995.

[3] W.G. Choi Le, S.B. Lee, D.D.Y. Ryu, Biotechnol. Bioeng. 23 (1981) 361.

[4] D.H. Nam, C. Kim, D.D.Y. Ryu, Biotechnol. Bioeng. 27 (1985) 953.

[5] L. Crawford, A.M. Stepan, P.C. McAda, J.A. Rambosek, M.J. Conder, V.A. Vinci, C.D. Reeves, Bio/Technology 13 (1995) 58.

[6] M. Nieboer, E. de Vroom, J. Lugtenburg, D. Schipper, A. Vollebregt, R. Bovenberg, Pat. WO 98/48034 (1998).

[7] I.A.L.A. Boogers, E.J.A.X. van de Sandt, D. Schipper, Pat. WO 99/50271 (1999).

[8] E.J.A.X. Van de Sandt, E. de Vroom, Chim. Oggi 18 (2000) 72.

[9] A.C. Ghosh, R.K. Mathur, N.N. Dutta, Adv. Biochem. Eng./ Biotechnol. 56 (1997) 111.

[10] F. Helfferich, G. Klein, Multicomponent Chromatography – Theory of Interference, Marcel Dekker, New York, 1970.

[11] H. Rhee, R. Aris, N.R. Amundson, Phil. Trans. Royal Soc. A 267 (1970) 419.

[12] W. Fritz, E.-U. Schluender, Chem. Eng. Sci. 29 (1974) 1279.

[13] P.C. Wankat, Rate-Controlled Separations, Blackie, London, 1994.

[14] D.D. Frey, A. Barnes, J.C. Strong, AIChE J. 41 (1995) 1171.

[15] C.R. Narahari, J.C. Strong, D.D. Frey, J. Chromatogr. A 825 (1998) 115.

[16] R.C. Bates, D.D. Frey, J. Chromatogr. A 814 (1998) 43.

[17] P.J. Schoenmakers, H.A.H. Billiet, R. Tijssen, L. de Galan, J. Chromatogr. 149 (1978) 519.

[18] L.R. Snyder, J.W. Dolan, J.R. Gant, J. Chromatogr. 165 (1979) 3.

[19] F.D. Antia, Horvath, J. Chromatogr. 484 (1989) 1.

[20] E.I. Franses, F.A. Siddiqui, D.J. Ahn, C.H. Chang, N.-H.L. Wang, Langmuir 11 (1995) 3177.

[21] Z. Ma, R.D. Whitley, N.-H.L. Wang, AIChE J. 42 (1996) 1244.

[22] B.J. Hritzko, D.D. Walker, N.-H.L. Wang, AIChE J. 46 (2000) 552.

[23] C. Migliorini, M. Mazzotti, M. Morbidelli, AIChE J. 45 (1999) 1411.

[24] Y. Xie, D. Wu, Z. Ma, N.-H.L. Wang, Ind. Eng. Chem. Res. 39 (2000) 1993.

[25] C.R. Wilke, P.I.N. Chang, AIChE J. 1 (1955) 264.

[26] B.J. Hritzko, M.J. Ortiz-Vega, N.-H.L. Wang, Ind. Eng. Chem. Res. 38 (1999) 2754.

[27] R.A. Robinson, R.H. Stokes, Electrolyte Solution, Butterworths, London, 1955.

[28] E.J. Wilson, C.J. Geankoplis, Ind. Eng. Chem. Fundam. 5 (1966) 9.

[29] S.F. Chung, C.Y. Wen, AIChE J. 14 (1968) 857.

[30] J.S. Mackie, P. Meares, Proc. Royal Soc. London Ser. A 232 (1955) 498.

[31] Q. Yu, N.-H.L. Wang, Comput. Chem. Eng. 13 (1989) 915.

[32] R.D. Whitley, Ph.D. Thesis, Purdue University, West Lafayette, IN, December 1990.

[33] J.A. Berninger, R.D. Whitley, X. Zhang, N.-H.L. Wang, Comput. Chem. Eng. 15 (1991) 749.

[34] J.V. Villadsen, M.L. Michelsen, Solution of Differential Equation Models by Polynomial Approximation, Prentice-Hall, Englewood Cliffs, NJ, 1978.

[35] B.A. Finlayson, Nonlinear Analysis in Chemical Engineering, McGraw-Hill, New York, 1980.

[36] L.R. Petzold, DASSL: A Differential/Algebraic System Solver, Lawrence Livermore National Laboratory, Livermore, CA, 1982.

[37] M.V. Chaubal, G.F. Payne, C.H. Reynolds, R.L. Albright, Biotechnol. Bioeng. 47 (1995) 215.

[38] S.U. Kim, J.A. Berninger, Q. Yu, N.-H.L. Wang, Ind. Eng. Chem. Res. 31 (1992) 1717.